Energy-Optimal Low-Thrust Control of Constrained Relative Motion for Long-Term Spacecraft Hovering

Chuncheng Zhao [1], Michele Maestrini [1], Pierluigi Di Lizia [1]

[1] *Polytechnic University of Milan*
Milan, Italy
Email: chuncheng.zhao@polimi.it, michele.maestrini@polimi.it, pierluigi.dilizia@polimi.it.

Abstract – **Future space missions have raised the demand for efficient and reliable control strategies to carry out proximity operations, and the increasing application of small satellites, such as CubeSats, has imposed more constraints on control algorithms. Focusing on spacecraft relative hovering, which is an important phase for proximity operations around near-Earth space, this paper proposes both energy-optimal low-thrust maneuvers and target selection strategies to enable long-term hovering missions while minimizing fuel consumption. Analytical solutions are provided for two energy-optimal control scenarios: general thrust and constrained thrust cases, where the latter caters to underactuated satellites. Moreover, this paper designs constrained periodic orbits with adjustable parameters and conducts statistical analyses to assess their impact on hovering duration within a defined region. A target periodic orbit is identified based on the performance of residence time inside the hovering region, and then target points on the chosen periodic orbit are assessed to determine an optimal one in terms of both residence time and fuel cost. Finally, a strategy for achieving long-term hovering is outlined through multiple cycles of drifting and control phases, with an optimal target point determined at the start of each control phase. Numerical simulations are performed to validate the effectiveness and robustness of the proposed methods at each stage.**

I. INTRODUCTION

Near-Earth space missions, encompassing activities such as active space debris removal and on-orbit servicing, have garnered increasing interest from both public organizations aiming to expand human capabilities and private initiatives seeking to engage in commercial space activities [1]. Proximity operations of spacecraft, including rendezvous and inspection, play a crucial role in these missions and have been extensively researched in recent decades [2]. One pivotal phase in spacecraft proximity operations is relative hovering, where a controllable spacecraft maintains a safe position in proximity to a target spacecraft [3]. This phase allows for the reception of commands or the acquisition of additional information before proceeding further.

Initially, the control law was designed to keep spacecraft hovering at a fixed relative position with respect to the target in the Local-Vertical-Local-Horizontal (LVLH) frame [4]. Based on the design of periodic relative orbits, which can be naturally periodic without perturbations,

as well as the need for control [5], most researchers started work on designing controls to keep the relative motion in a bounded region [6]. This paper investigates the long-term hovering problem based on the search for constrained periodic orbits. Instead of focusing on the well-established approach of impulsive control [6-7], this paper deals with a specific hovering problem by low-thrust continuous control, involving a natural drifting stage within a bounded region due to perturbations and a following controlled stage that brings the relative state to a predefined target point on a target periodic orbit [8].

This study designs energy-optimal low-thrust controls, along with selecting the optimal target point, aimed at executing long-term hovering missions and minimizing fuel costs. Energy-Optimal Control Problems (EOCP) are solved analytically for two cases: general thrust and constrained tangential thrust. The latter is valuable for underactuated satellites like CubeSats, which have limited control actuation capacity [9]. Next, constrained periodic orbits are designed with variable parameters and validated through sensitivity analyses. Statistical analyses of periodic orbits are then presented to evaluate the impact of parameters on the drifting time within a specified hovering region. A periodic orbit can be identified by its performance, such as residence time inside a hovering region. Following this, points on the chosen periodic orbit are assessed to determine the optimal one regarding drifting time and fuel cost. The concept of long-term hovering is realized by the concatenation of multiple cycles of drifting and control phases, with an optimal target point assigned at the beginning of each control phase. The design of constrained periodic orbits and the selection of an optimal target point enable the trade-off between fuel cost and useful hovering time, proving particularly beneficial for small satellites with limited resources seeking to perform extended tasks. Finally, numerical simulations are conducted to verify the efficiency and robustness of the proposed approaches for long-term hovering under different parameters of spacecraft orbits. These simulations serve to validate the practicality and effectiveness of the presented methods.

The paper is organized as follows: First, dynamical models are presented to design the solution to the optimal control problems and introduce periodic relative orbits. Then, an analytical method is given to solve EOCPs with both general and tangential thrust. Next, the selection of the target periodic orbit and optimal target point are discussed for carrying out long-term hovering.

II. DYNAMICAL MODELS

In this paper, considering relative motion between two spacecrafts, the passive spacecraft which is the object of proximity operations will be referred to as the leader, and the active spacecraft that can perform maneuvers will instead be called the follower. As shown in Fig.1, the LVLH frame which is centered on the mass center of the leader S_l is denoted by $\{S_l, i, j, k\}$. The Earth-Centered Inertial (ECI) frame is denoted by $\{O, I, J, K\}$. It is noted that k is the radial vector and is positive toward the center of the Earth O, j is the cross-track vector opposite to the orbit angular momentum, and i is the in-track vector satisfying the right-handed rule. The relative position ρ of the follower S_f is expressed in the LVLH frame, while r_f and r_l represent the inertial positions of the two spacecrafts in the ECI frame.

The inertial dynamic for the follower is chosen for the control design since this model is more convenient to retrieve analytical solutions for the EOCP. Based on the assumption of Keplerian motion and the supposition that the change in the follower's mass is negligible, the inertial dynamic can be written in the ECI frame as,

$$\begin{cases} \dot{r} = v \\ \dot{v} = -\dfrac{\mu}{r^3} r + a_c \end{cases} \quad (1)$$

where μ is Earth's gravitational constant. Throughout this paper, the vector $[r; v]$ refers to the inertial states of follower omitting the subscript f. a_c is the control acceleration term. In addition, a model from [10] is used to simulate the realistic non-linear disturbed relative motion for the simulations carried out in Sections III and IV. While this model relies on the propagation of perturbed orbital elements according to Gauss planetary equations, it is simple to use it even in the presence of a control acceleration.
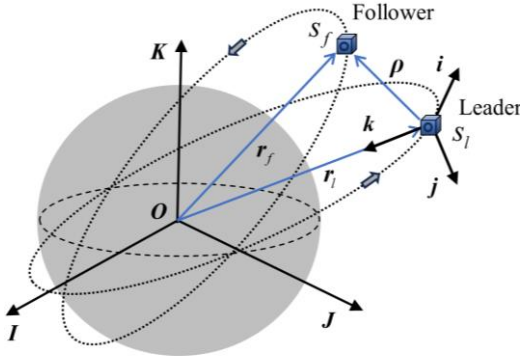
Fig. 1. Inertial Earth-centered frame and LVLH frame.

Considering that the distance between the leader and the follower spacecrafts is much smaller than the distance between the leader and the Earth's center (i.e., $\|r_l\| \gg \|\rho\|$), the relative dynamic expressed in the LVLH frame can be described as a state-space representation using linearized Tschauner–Hempel equations [11],

$$\dot{X}(t) = A(t)X(t) \quad (2)$$

where the state vector X represents the relative states, $X(t) = [x(t); y(t); z(t); v_x(t); v_y(t); v_z(t)]$. Then, after a similarity transformation from relative states $X(t)$ with independent variable time t to relative states $X^*(\nu)$ with true anomaly ν is applied, the Yamanaka-Ankersen state transition matrix [12] can be used for the propagation of relative motion from an initial state $X^*(\nu_0)$,

$$X^*(\nu) = \Phi(\nu, \nu_0)X^*(\nu_0) \quad (3)$$

Expanding (3) and factoring out the terms associated with the independent variable ν, the equations of relative position can be expressed as,

$$x^*(\nu) = (2 + e\cos\nu)(d_1(\nu_0)\sin\nu$$
$$-d_2(\nu_0)\cos\nu + d_3(\nu_0) + 3d_0(\nu_0)J(\nu,\nu_0)(1+e\cos\nu)^2$$
$$y^*(\nu) = d_4(\nu_0)\cos\nu + d_5(\nu_0)\sin\nu \quad (4)$$
$$z^*(\nu) = (1 + e\cos\nu)(d_1(\nu_0)\cos\nu + d_2(\nu_0)\sin\nu)$$
$$-3ed_0(\nu_0)J(\nu,\nu_0)\sin\nu(1+e\cos\nu) + 2d_0(\nu_0)$$

where $J(\nu, \nu_0)$ is an integral term, and the specific expression can be found in [6]. The parameters $d_i(\nu_0)$ with $i = (0, 1, 2, 3, 4, 5)$ are the factored terms. Inspired by (4), the concept of the vector of parameters $D(\nu) = [d_0(\nu); d_1(\nu); d_2(\nu); d_3(\nu); d_4(\nu); d_5(\nu)]$ was proposed in [5] to represent relative states. By looking at (4), it can be noticed that the relative motion in the out-of-plane direction is naturally periodic. Conversely, to obtain periodic motion in-plane the parameter $d_0(\nu_0)$ must be set to 0, which eliminates the effect of the drifting term $J(\nu, \nu_0)$. Therefore, the periodicity condition of relative motion at the initial moment is $d_0(\nu_0) = 0$, and then (4) can be simplified to design periodic relative orbits with set orbit boundaries as was presented in [8].

III. ENERGY-OPTIMAL LOW-THRUST CONTROL

This section is dedicated to mathematical developments to retrieve the optimal control solutions to the hovering problem. The mathematical derivation of an analytical method for the design of low-thrust energy-optimal control will be presented, which is based on the work from [13]. First, the solution in the case of general thrust is thoroughly presented. Next, the tangential thrust case is derived by constraining the acceleration direction.

A. General thrust

For the controlled motion of the follower, the inertial dynamic is written as,

$$\begin{cases} \dot{r} = v \\ \dot{v} = -\dfrac{\mu}{r^3} r + a_c \end{cases} \quad \text{Initial Conditions:} \begin{cases} r(t_0) = r_0 \\ v(t_0) = v_0 \end{cases} \quad (5)$$

where t_0 is the initial time, and r_0 and v_0 are the initial inertial position and velocity respectively. The cost function that the EOCP tries to minimize is defined as,

$$J = \frac{1}{2}\int_{t_0}^{t_f} a_c^T a_c \, dt \quad (6)$$

where t_f is the terminal time. Thus, the Hamiltonian is,

$$H = \frac{1}{2}\boldsymbol{a}_c^{\mathrm{T}}\boldsymbol{a}_c + \boldsymbol{\lambda}_r^{\mathrm{T}}\boldsymbol{v} + \boldsymbol{\lambda}_v^{\mathrm{T}}\left(-\frac{\mu}{r^3}\boldsymbol{r} + \boldsymbol{a}_c\right) \qquad (7)$$

In this expression $\boldsymbol{\lambda}_r$ and $\boldsymbol{\lambda}_v$ represent the costates. From Pontryagin's minimum principle [14], the optimal control law is the one minimizing the Hamiltonian, which yields,

$$\boldsymbol{a}_c^* = -\boldsymbol{\lambda}_v \qquad (8)$$

Given fixed final states [$\boldsymbol{r}_f$; $\boldsymbol{v}_f$], this EOCP can be written as follows adopting the Euler-Lagrange equations [14],

$$\begin{cases} \dot{\boldsymbol{r}} = \boldsymbol{v} \\ \dot{\boldsymbol{v}} = -\dfrac{\mu}{r^3}\boldsymbol{r} - \boldsymbol{\lambda}_v \\ \dot{\boldsymbol{\lambda}}_r = \dfrac{\mu}{r^3}\boldsymbol{\lambda}_v - \dfrac{3\mu\boldsymbol{r}\cdot\boldsymbol{\lambda}_v}{r^5}\boldsymbol{r} \\ \dot{\boldsymbol{\lambda}}_v = -\boldsymbol{\lambda}_r \end{cases} \text{Boundaries:} \begin{cases} \boldsymbol{r}(t_0) = \boldsymbol{r}_0 \\ \boldsymbol{v}(t_0) = \boldsymbol{v}_0 \\ \boldsymbol{r}(t_f) = \boldsymbol{r}_f \\ \boldsymbol{v}(t_f) = \boldsymbol{v}_f \end{cases} (9)$$

This is a typical Two-Point-Boundary-Value-Problem (TPBVP) with a given time window [t_0, t_f]. Instead of solving it iteratively with computationally expensive methods whose convergence is highly affected by the first guess solution, this TPBVP can be transformed into an Initial Value Problem (IVP) aiming to find the initial costates ($\boldsymbol{\lambda}_{r0}$, $\boldsymbol{\lambda}_{v0}$). To achieve this aim, Equation (9) is linearized around the nominal uncontrolled dynamics, and the State Transition Matrix (STM) $\boldsymbol{\Phi}$ is employed to analytically propagate variations of initial states and costates within the given time frame. The STM can be computed from the following set of ordinary differential equations,

$$\dot{\boldsymbol{\Phi}}(t,t_0) = \mathbf{A}(t)\boldsymbol{\Phi}(t,t_0), \ \boldsymbol{\Phi}(t_0,t_0) = \mathbf{I}_{n\times n} \qquad (10)$$

where $\mathbf{A}$ is the Jacobian of the dynamics system expressed in (9) and evaluated on the nominal Keplerian as in [13]. Next, the variations of initial states are linearly mapped into variations of final states thanks to the STM,

$$\begin{bmatrix} \delta\boldsymbol{r}_f \\ \delta\boldsymbol{v}_f \\ \delta\boldsymbol{\lambda}_{rf} \\ \delta\boldsymbol{\lambda}_{vf} \end{bmatrix} = \begin{bmatrix} \boldsymbol{\Phi}_{11} & \boldsymbol{\Phi}_{12} & \boldsymbol{\Phi}_{13} & \boldsymbol{\Phi}_{14} \\ \boldsymbol{\Phi}_{21} & \boldsymbol{\Phi}_{22} & \boldsymbol{\Phi}_{23} & \boldsymbol{\Phi}_{24} \\ \boldsymbol{\Phi}_{31} & \boldsymbol{\Phi}_{32} & \boldsymbol{\Phi}_{33} & \boldsymbol{\Phi}_{34} \\ \boldsymbol{\Phi}_{41} & \boldsymbol{\Phi}_{42} & \boldsymbol{\Phi}_{43} & \boldsymbol{\Phi}_{44} \end{bmatrix} \begin{bmatrix} \delta\boldsymbol{r}_0 \\ \delta\boldsymbol{v}_0 \\ \delta\boldsymbol{\lambda}_{r0} \\ \delta\boldsymbol{\lambda}_{v0} \end{bmatrix} (11)$$

Given that the initial states are fixed, $\delta\boldsymbol{r}_0 = 0$ and $\delta\boldsymbol{v}_0 = 0$, the previous expression can be simplified. Moreover, since the costates are zero on the nominal trajectory, then $\delta\boldsymbol{\lambda} = \boldsymbol{\lambda}$ at all times. Meanwhile, the variations of the final states are imposed given that specific target position and velocity are required to achieve the desired target state on a relative periodic orbit: $\delta\boldsymbol{r}_f = \boldsymbol{r}_f - \boldsymbol{r}_p$, $\delta\boldsymbol{v}_f = \boldsymbol{v}_f - \boldsymbol{v}_p$. Here $\boldsymbol{r}_p$ and $\boldsymbol{v}_p$ represent the final nominal states obtained from the propagation of Keplerian motion. Extracting the first two lines from (11),

$$\begin{aligned} \delta\boldsymbol{r}_f &= \boldsymbol{\Phi}_{13}\boldsymbol{\lambda}_{r0} + \boldsymbol{\Phi}_{14}\boldsymbol{\lambda}_{v0} \\ \delta\boldsymbol{v}_f &= \boldsymbol{\Phi}_{23}\boldsymbol{\lambda}_{r0} + \boldsymbol{\Phi}_{24}\boldsymbol{\lambda}_{v0} \end{aligned} \qquad (12)$$

Then, the analytical solution of initial costates can be obtained as,

$$\begin{aligned} \boldsymbol{\lambda}_{r0} &= \boldsymbol{\Phi}_{13}^{-1}(\delta\boldsymbol{r}_f - \boldsymbol{\Phi}_{14}\boldsymbol{\lambda}_{v0}) \\ \boldsymbol{\lambda}_{v0} &= (\boldsymbol{\Phi}_{24} - \boldsymbol{\Phi}_{23}\boldsymbol{\Phi}_{13}^{-1}\boldsymbol{\Phi}_{14})^{-1}(\delta\boldsymbol{v}_f - \boldsymbol{\Phi}_{23}\boldsymbol{\Phi}_{13}^{-1}\delta\boldsymbol{r}_f) \end{aligned} (13)$$

When $\boldsymbol{r}_f$, $\boldsymbol{r}_p$, $\boldsymbol{v}_f$ and $\boldsymbol{v}_p$ are known, the initial costates can be directly calculated by solving (13). The integration of the Keplerian and STM dynamics only needs to be carried out once in the desired time window, which significantly reduces computational time. It should be noted that the desired target final states of the control are expressed as relative states on a periodic relative orbit, hence they are expressed in the LVLH frame. Nonetheless, since the final inertial states of the leader can be immediately propagated to the desired end time of the control, the target final inertial states [$\boldsymbol{r}_f$; $\boldsymbol{v}_f$] of the follower can be easily obtained to retrieve the needed inputs for the solution.

B. Tangential thrust

The previously discussed solution of the EOCP with unbounded control direction presents some difficulties in terms of implementation on CubeSats with limited actuation capacity. Therefore, this issue may be mitigated by constraining the input to lie in a specific direction. For this case, the control thrust is constrained to be tangential, hence aligned with the vector $\boldsymbol{v}/v$. Then, by inserting this constraint into the dynamics expressed in (5), the new model becomes,

$$\begin{cases} \dot{\boldsymbol{r}} = \boldsymbol{v} \\ \dot{\boldsymbol{v}} = -\dfrac{\mu}{r^3}\boldsymbol{r} + a_t\dfrac{\boldsymbol{v}}{v} \end{cases} \text{Initial Conditions:} \begin{cases} \boldsymbol{r}(t_0) = \boldsymbol{r}_0 \\ \boldsymbol{v}(t_0) = \boldsymbol{v}_0 \end{cases} (14)$$

Here $\boldsymbol{a}_c = a_t\boldsymbol{v}/v$, and a_t is the magnitude of tangential control acceleration. Because of the limit of acceleration direction, the cost function will change by replacing $\boldsymbol{a}_c$ with $a_t\boldsymbol{v}/v$. The tangential thrust is applied in the orbital plane of the follower, so that the out-of-plane target relative state, the $\boldsymbol{j}$ direction of LVLH, cannot be reached through tangential control. Moreover, the periodicity condition of relative motion is only related to in-plane states [8]. Therefore, four equations of finial in-plane state constraints are included in the formulation of the optimal control problem,

$$\psi(\boldsymbol{X}_f) = \begin{cases} x_f - x_t = 0 \\ z_f - z_t = 0 \\ v_{xf} - v_{xt} = 0 \\ v_{zf} - v_{zt} = 0 \end{cases} \qquad (15)$$

where [x_f, z_f, v_{xf}, v_{zf}] are the final in-plane states at the end of control and [x_t, z_t, v_{xt}, v_{zt}] are the target final in-plane states on a periodic orbit. Then, the augmented cost function becomes [14],

$$J' = \boldsymbol{\kappa}^{\mathrm{T}}\psi(\boldsymbol{X}_f) + \frac{1}{2}\int_{t_0}^{t_f} a_t^2 dt \qquad (16)$$

where $\boldsymbol{\kappa}$ is a vector of Laplace multipliers. Here, the Hamiltonian is,

$$H = \frac{1}{2} a_t^2 + \boldsymbol{\lambda}_r^{\mathrm{T}} \boldsymbol{v} + \boldsymbol{\lambda}_v^{\mathrm{T}} \left(-\frac{\mu}{r^3} \boldsymbol{r} + a_t \frac{\boldsymbol{v}}{v} \right) \qquad (17)$$

where the only controllable variable is a_t. Similarly, from Pontryagin's minimum principle, the optimal control law yields,

$$a_t^* = -\boldsymbol{\lambda}_v \cdot \frac{\boldsymbol{v}}{v} \qquad (18)$$

Then, this EOCP can be formulated as [14],

$$\begin{cases} \dot{\boldsymbol{r}} = \boldsymbol{v} \\ \dot{\boldsymbol{v}} = -\frac{\mu}{r^3} \boldsymbol{r} - \left(\boldsymbol{\lambda}_v \cdot \frac{\boldsymbol{v}}{v} \right) \frac{\boldsymbol{v}}{v} \\ \dot{\boldsymbol{\lambda}}_r = \frac{\mu}{r^3} \boldsymbol{\lambda}_v - \frac{3\mu \boldsymbol{r} \cdot \boldsymbol{\lambda}_v}{r^5} \boldsymbol{r} \\ \dot{\boldsymbol{\lambda}}_v = -\boldsymbol{\lambda}_r + \frac{\boldsymbol{\lambda}_v \cdot \boldsymbol{v}}{v^2} \left(\boldsymbol{\lambda}_v - \frac{\boldsymbol{\lambda}_v \cdot \boldsymbol{v}}{v^2} \boldsymbol{v} \right) \end{cases} \qquad (19)$$

$$\text{Boundaries:} \begin{cases} \boldsymbol{r}(t_0) = \boldsymbol{r}_0 \\ \boldsymbol{v}(t_0) = \boldsymbol{v}_0 \\ \boldsymbol{\lambda}_r(t_f) = \dfrac{\partial (\boldsymbol{\kappa}^{\mathrm{T}} \boldsymbol{\psi}(X_f))}{\partial \boldsymbol{r}_f} \\ \boldsymbol{\lambda}_v(t_f) = \dfrac{\partial (\boldsymbol{\kappa}^{\mathrm{T}} \boldsymbol{\psi}(X_f))}{\partial \boldsymbol{v}_f} \end{cases}$$

The Jacobian matrix **A** of the above dynamics system was given in [8]. The mapping variation from initial states into final states with STM is the same as (11), and it is expanded to,

$$\begin{cases} \delta \boldsymbol{r}_f = \boldsymbol{\Phi}_{13} \boldsymbol{\lambda}_{r0} + \boldsymbol{\Phi}_{14} \boldsymbol{\lambda}_{v0} \\ \delta \boldsymbol{v}_f = \boldsymbol{\Phi}_{23} \boldsymbol{\lambda}_{r0} + \boldsymbol{\Phi}_{24} \boldsymbol{\lambda}_{v0} \\ \boldsymbol{\lambda}_{rf} = \boldsymbol{\Phi}_{33} \boldsymbol{\lambda}_{r0} + \boldsymbol{\Phi}_{34} \boldsymbol{\lambda}_{v0} \\ \boldsymbol{\lambda}_{vf} = \boldsymbol{\Phi}_{43} \boldsymbol{\lambda}_{r0} + \boldsymbol{\Phi}_{44} \boldsymbol{\lambda}_{v0} \end{cases} \qquad (20)$$

Including the boundary condition of final costates and final in-plane state constraints, Equation (20) is extended to a new system of equations,

$$\begin{cases} \delta \boldsymbol{r}_f - \boldsymbol{\Phi}_{13} \boldsymbol{\lambda}_{r0} - \boldsymbol{\Phi}_{14} \boldsymbol{\lambda}_{v0} = 0 \\ \delta \boldsymbol{v}_f - \boldsymbol{\Phi}_{23} \boldsymbol{\lambda}_{r0} - \boldsymbol{\Phi}_{24} \boldsymbol{\lambda}_{v0} = 0 \\ \dfrac{\partial (\boldsymbol{\kappa}^{\mathrm{T}} \boldsymbol{\psi}(X_f))}{\partial \boldsymbol{r}_f} - \boldsymbol{\Phi}_{33} \boldsymbol{\lambda}_{r0} - \boldsymbol{\Phi}_{34} \boldsymbol{\lambda}_{v0} = 0 \\ \dfrac{\partial (\boldsymbol{\kappa}^{\mathrm{T}} \boldsymbol{\psi}(X_f))}{\partial \boldsymbol{v}_f} - \boldsymbol{\Phi}_{43} \boldsymbol{\lambda}_{r0} - \boldsymbol{\Phi}_{44} \boldsymbol{\lambda}_{v0} = 0 \\ \boldsymbol{\psi}(X_f) \end{cases} \qquad (21)$$

This system includes 16 equations with 16 unknowns $[\boldsymbol{r}_f, \boldsymbol{v}_f, \boldsymbol{\lambda}_{r0}, \boldsymbol{\lambda}_{v0}, \boldsymbol{\kappa}]$. After the initial costates are found from (21), the IVP can be integrated to get the optimal control history and optimal trajectory.

C. Numerical simulations

Some simulations are conducted to demonstrate the efficacy of the control methods proposed in this section. The Simulink model in [10] is adopted as a ground truth dynamical model which is based on the nonlinear Gauss variational equations including Earth J_2 oblateness effect and atmospheric drag as perturbation sources. The two spacecrafts' initial orbit elements and parameters used for simulations are the same as in [8], as well as the defined hovering zone. Fig. 2 shows the results of the propagation from these initial conditions until the disturbed trajectory arrives at the boundary of the hovering region. Once the disturbed motion reaches the boundary, the control is adopted to bring the follower back to a relative periodic orbit that lies inside the admissible region.

For this preliminary validation, the initial periodic relative orbit is adopted as the target of the control. By further setting the control time to 1 orbital period of the leader, the target point is also fixed. The details about the design of an optimal target point will be discussed in Section IV. Next, the EOCPs are solved and simulated with unperturbed dynamics to demonstrate the ability to reach the desired conditions with the designed controls. In subsequent analyses, the perturbations will be added and their effect during control will be assessed.

Fig. 3 shows an example of the solution achieved by the proposed methods. It is visually evident from Fig. 3 (a) and (b) that the tangential control ends at a final point which has an error in the y state with respect to the target point. This behavior is expected since the thrust is indeed bound to be executed in the tangential direction of the follower. However, given the small magnitude of the relative states, the leader and follower exhibit very similar orbital elements, which results in a control authority that is approximately exerted in the *i-k* plane of the LVLH frame. Consequently, the out-of-plane component cannot be fully controlled. It is noticed from Fig. 3 (c) that the sign of the acceleration magnitude of tangential control changes during the control phase, which implies the change of thrust direction along positive and negative tangential directions.
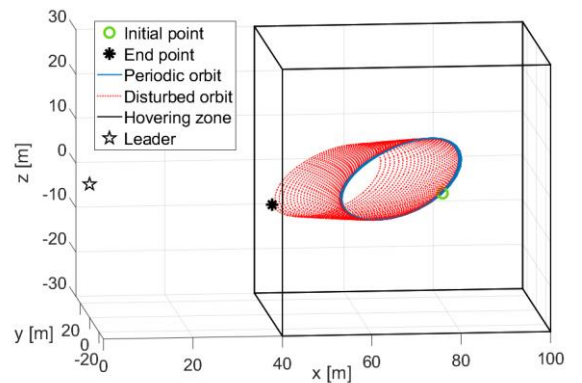
Fig. 2. Simulation of disturbed motion
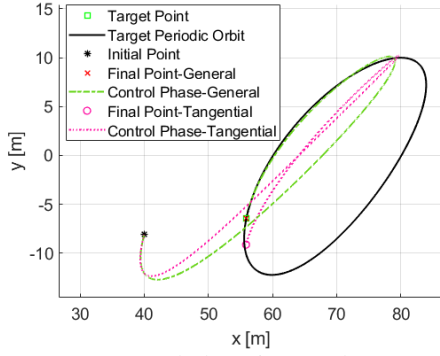
(a) Control phase in x-y plane
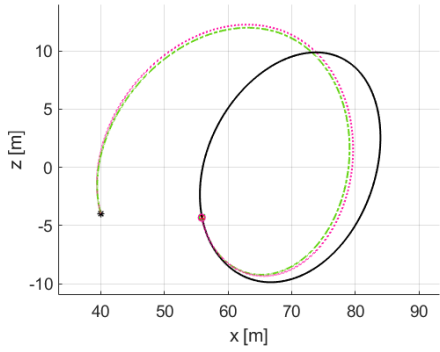
(b) Control phase in x-z plane
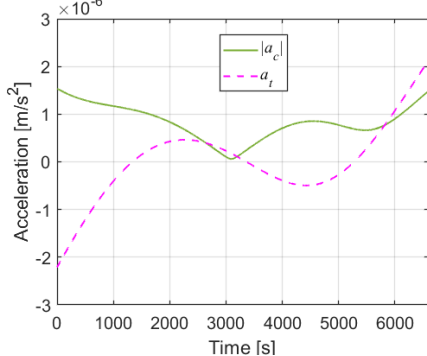
(c) Control profile

Fig.3. Comparison of general and tangential control

IV. LONG-TERM HOVERING CONTROL

The strategy to perform long-term hovering control is developed in this section. The key idea is to design and execute a control action every time the follower spacecraft exits the hovering region due to the presence of orbital perturbations. To do so, the operations are divided into two main phases: a drifting phase, also named the hovering phase, and a control phase. The former is defined as a phase of uncontrolled relative motion inside the hovering region. The latter is defined as the controlled phase that brings the spacecraft from the boundary of the hovering region to the desired target relative states. These two phases together form one cycle, and long-term hovering control can be achieved via multiple consecutive cycles. Considering some performance metrics such as fuel consumption and the

duration of drifting phases, the target periodic orbit and corresponding optimal target point can then be selected and evaluated so that target relative states can be provided to the optimal control design during each cycle. In fact, the longer the drift time between cycles, the smaller the number of maneuvers necessary and hence their cumulative cost to perform a longer mission. Moreover, reducing the need for maneuvers allows for longer operational phases. To better clarify the long-term hovering procedure, the cycle to conduct operations is presented in Fig. 4.
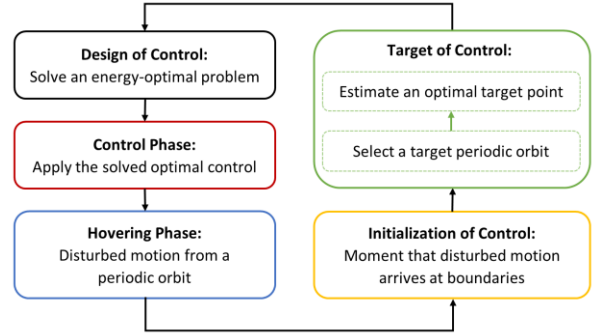
Fig.4. Overview of long-term hovering

A. Target periodic orbit

An algorithm was proposed to solve constrained periodic orbits in [8], based on the parameter description of space-restricted periodic trajectories and polynomial inequalities [6]. This algorithm is capable of dealing with upper and lower bounds on the size of the orbit and with a prescribed location for the center of the orbit. Here, this algorithm is applied to find a relative periodic orbit. Subsequently, statistical analyses of the impact of the periodic orbit's dimension and position on the drifting duration inside the hovering zone are carried out to determine an adequate target periodic orbit.

The feasibility of the proposed algorithm that is solved by fmincon is verified with a series of tests. First, the x-center is fixed at the center of the hovering region, e.g., 70 m, while the orbit eccentricity of the leader is set at $e = 0.1$. Orbit's z boundary is gradually enlarged from 1 m to 17 m with a 4 m difference, and Orbit's y boundary is fixed at 5 m. The change of the solved orbit's x boundary with respect to the change of the z boundary is shown in Fig. 5. This test shows that the x range of the solved orbit will increase as the z boundary increases. However, when the x boundary of the orbit arrives at the boundary of the hovering zone for the first time, the algorithm is not able to get a feasible solution. Second, the orbit's z and y boundaries are fixed at 5 m, and the effect of orbit eccentricity on the solved orbit is shown in Fig. 6 with $e = [1 \times 10^{-4}, 0.05, 0.1, 0.2, 0.3]$. This figure shows that the orbit's x boundary of the solved orbit mostly enlarges with the increase of e.

Within a given hovering zone, there are infinitely many periodic orbits. It would be computationally intensive to directly search for an optimal periodic orbit which

maximizes the drift time. Hence, the statistical analyses are conducted for the impact of the periodic orbit's shape on the drift duration. These analyses will provide valuable guidelines for the choice of target periodic orbit for the long-term hovering mission. After performing several simulations, some general trends emerged. The first thing that appeared from this investigation is that for longer propagations the drag will become the main influence compared to J_2. This is expected due to the gradual accumulation of velocity changes imposed by this non-conservative perturbation. Secondly, the drift caused by the drag is always in the same direction as the LVLH frame if the coefficients of two spacecrafts are fixed. Therefore, the drift direction of the disturbed motion will follow the drift caused by the drag if the duration is long enough. Third, the hovering boundary region will always be violated in the i direction of the LVLH frame if the y and z boundaries of the periodic orbit are not too close to the boundaries of the hovering zone. Therefore, the following analyses will specifically focus on the motion in the i direction.

Different parameters of the relative orbit are varied to assess their impacts on the drift time. However, the eccentricity is fixed at 0.1 for next analyses. Firstly, it is to determine the impact of the in-plane size. The x-center is fixed at 70 m, and the y boundary is fixed at 5 m. Subsequently, the orbit's z boundary is enlarged from 1 m to 10 m with a 3 m difference. 10 different target points within 1 period control time window are picked from each periodic orbit as the starting point of a simulation to retrieve their drift time under perturbations of J_2 and drag. The results are shown in Fig. 7. It can be noticed that, as the in-plane size grows, the drift time will decrease. This behavior can easily be imputed to the fact that the distance between the x boundary of the hovering zone and the periodic orbit will decrease. Secondly, the effect of the orbit's x-center is analyzed. Since the orbit's y and z centers are 0 and the drift is mainly along i direction, only the x position of the periodic orbit is analyzed. Here, y and z boundaries are fixed at 5 m. The x-center is changed from 57 m to 81 m with steps of 8 m, and the orbit's x boundary is retrieved with the mentioned algorithm. The simulated drift time is given in Fig. 8. In this case, because the drift direction of drag is along the negative i direction, the drift time will increase as the x-center moves toward the positive i direction. However, when the x-center is enlarged to a certain value, the disturbed motion starting from some points may end at the upper boundary of the hovering region. This is caused by the fact that the main influence starting from these points is given by J_2 perturbation. This trend is clearly observable in Fig. 8, and it is verified at points 0.5, 0.9, and 1 period when the x-center is 81 m. Moreover, if the drift direction of drag is along the positive i direction, it is reasonable to state that the drift time will decrease as the x-center moves toward the positive i direction.

To sum up the results, the larger the size of the periodic orbit, the shorter the drift time. However, the size of the orbit cannot be reduced too much. In fact, it is essential that the follower has sufficient variation in viewing angle with respect to the leader for some operations. Hence, there should be a balance of different task demands to set adequate orbit boundary values. In view of enlarging the drift duration, it is desirable to locate the x center as far as possible in the opposite of the drag's drifting direction. Hereafter, we will consider the conservative choice to set x-center as the center of the hovering zone.
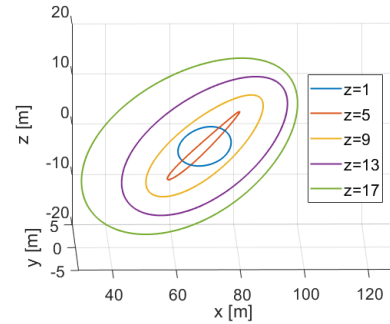
Fig.5. Periodic orbits of changed in-plane size.
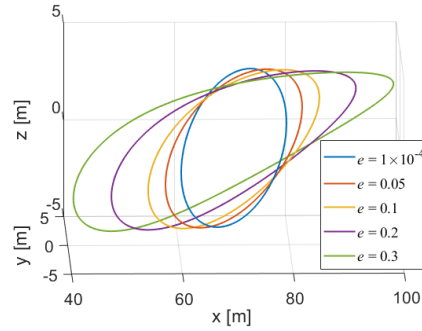
Fig.6. Periodic orbits of changed orbit eccentricity.
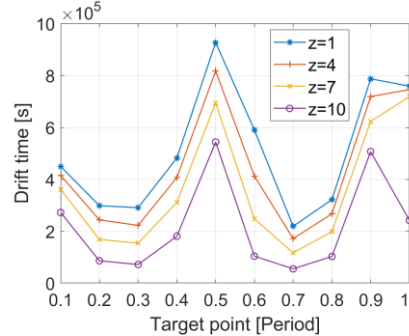
Fig. 7. Effects of orbit's in-plane size.
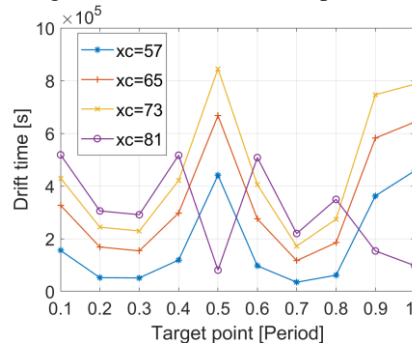
Fig. 8. Effects of orbit's x center (xc).

B. Optimal target point

From the above statistical analyses, it has been shown that disturbed motion starting from different points on a periodic orbit will have a different drift time for one cycle of long-term hovering strategy. After a target periodic orbit is designed, the optimal target point on this orbit should also be selected to provide it to the optimal control module. The target points should be evaluated considering the fuel cost and the drift time. The results in [8] showed that the fuel cost converges to a value after a control time of nearly 1 period. Therefore, it is suggested to choose a target point in the second period for the energy-optimal control case. For the above analyses, the drift time was retrieved by simulating the disturbed dynamics, but it is extremely time-consuming and hence this approach is not suitable for a limited resource system such as a CubeSat. Therefore, an estimation method based on the short-term propagation of disturbed dynamics was proposed to approximately predict the drift time in [8].

For the following analyses, the target periodic orbit is centered at [70; 0; 0], the z and y boundaries are set to 5 m, and the x boundary is solved by the algorithm. The analyses conducted in the previous section to estimate the drift time are based on simulations where the perturbed motion starts exactly from the points on a target periodic orbit. However, for tangential thrust the target y relative state cannot be reached exactly. Consequently, the following periodic orbit will be different from the target one in the out-of-plane direction. However, for different control durations leading to different target points on a target periodic orbit, the attained periodic orbit after tangential control will always coincide. For subsequent long-term hovering cycles, the orbital parameters of the leader will be different due to the presence of perturbations. However, the periodic orbit obtained by the algorithm with the same y and z boundaries is almost constant. This is explained by the fact that the only parameter impacting the shape of the periodic orbit is the leader's orbit eccentricity, which shows very little variation even in multiple hovering cycles. Nonetheless, the attained periodic orbits after tangential control in subsequent cycles will coincide with the target one in-plane but display different y boundaries. Indeed, the performed analyses show that this boundary increases with the number of cycles.

To simplify these analyses, perturbations are not activated during the control phase. Since the control is designed without perturbations, including the perturbations during the control phase would cause a final state error which would impact the drift time. As is seen in Fig. 9, the drift time obtained by the estimation method is almost the same for general and tangential cases at each control cycle. It is expected since the drift in the i direction is the main one and the x-z orbit boundary is decoupled from the y orbit boundary. Therefore, the estimated results from the general case,

which are much easier to compute, can be directly applied to the tangential case for the selection of the optimal target point.

C. Numerical simulations

In this section, the long-term hovering procedure is simulated in MATLAB and Simulink, with an i7-10700 2.90GHz CPU. The planning hovering horizon consists of 40 cycles within a general range of orbit eccentricity of the leader, like [1×10−4, 0.05, 0.1, 0.2], to verify the algorithm's effectiveness. The y and z orbit boundaries of the target periodic orbit are set at 5 m and the x-center is 70 m. Other parameters are the same as in [8].

The 40 cycles are simulated while the tangential thrust is adopted and the optimal target point is selected as the estimation point with the largest drift time. The cumulative fuel cost and drift time are plotted in Figs. 10 and 11. Table 1 reports the average time cost of the control design part for different orbit eccentricities.
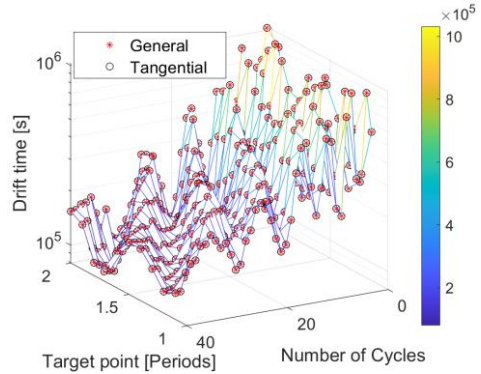
Fig.9. Comparison of the drift time for two cases
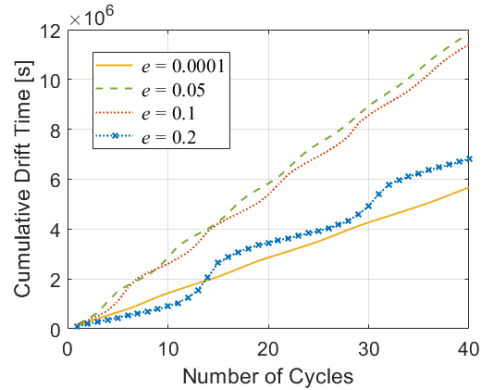
Fig.10. Cumulative drift time
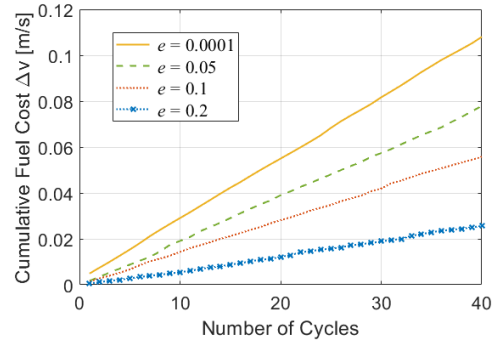
Fig.11. Cumulative fuel cost

Table 1. Average computational time used to design the control for long-term hovering.

	Orbit eccentricity			
	0.0001	0.05	0.1	0.2
Time [s]	0.115	0.098	0.101	0.096

It is seen that the larger the eccentricity, the smaller the total required cost. Conversely, the cumulative drift time does not have this trend as can be observed in Fig. 10. The cumulative drift time ranges from about 70 days for orbits with very small eccentricity to around 130 days for orbits with intermediate values of eccentricity. Curiously, the orbit with a larger value of eccentricity ($e = 0.2$) behaves similarly to the orbit that is almost circular in terms of cumulative drift time but at a much smaller cost. Overall, the average cost for a day of missions is 10^{-3} m/s per day. The time cost of EOCP is almost entirely within 0.1 seconds, proving the benefit of the analytical method.

From the simulations carried out, it can be concluded that the proposed methods are effective for different orbital eccentricities of the leader. Based on the analyses of periodic relative orbits and the estimation of the optimal target point, the drift time is maximized with low fuel costs. In addition, optimal control solutions can be rapidly obtained for EOCPs, benefiting from the analytical method.

V. CONCLUSION

This paper dealt with the challenging problem of providing a long-term control strategy for hovering in proximity of a target spacecraft, which is a fundamental task that is necessary to be performed before conducting other proximity operations. Firstly, two fully analytic energy-optimal control strategies were derived by considering both general thrust and the challenging case of only tangential thrust. The latter task makes the strategy more suitable for satellites with limited actuation capacity in terms of the number of engines. Secondly, this paper presented some statistical analyses considering the impact of the parameters of target periodic orbits on the duration of uncontrolled motion inside the hovering zone. Then, a fast approach to estimating the optimal target point on a periodic orbit is also evaluated. Finally, these steps are assembled into a cyclic procedure to perform a long-term hovering strategy that considers the insights provided by the previous analyses. The effort in both obtaining analytic solutions to reduce the computational effort and limiting the thrust in the tangential direction makes it a promising preliminary approach for the onboard application of an underactuated satellite.

VI. REFERENCES

[1] G. Genta, "Private space exploration: A new way for starting a spacefaring society?," *Acta Astronautica*, Vol. 104, No. 2, pp. 480-486, 2014.

[2] M. Maestrini, and P. Di Lizia, "Guidance Strategy for Autonomous Inspection of Unknown Non-Cooperative Resident Space Objects," *Journal of Guidance, Control, and Dynamics*, Vol. 45, No. 6, pp. 1126–1136, 2022.

[3] Z. Dang, Z. Wang, and Y. Zhang, "Modeling and Analysis of Relative Hovering Control for Spacecraft," J*ournal of Guidance, Control, and Dynamics*, Vol. 37, No. 11, pp. 1091–1102, 2014.

[4] H. Xu, Y. Ye, and Z. Yang, "Nonlinear Control of Underactuated Spacecraft Hovering," *Journal of Guidance, Control, and Dynamics*, Vol. 39, No. 3, pp. 685–694, 2016.

[5] G. Deaconu, C. Louembet, and A. Théron, "Designing Continuously Constrained Spacecraft Relative Trajectories for Proximity Operations," *Journal of Guidance, Control, and Dynamics*, Vol. 38, No. 7, pp. 1208–1217, 2015.

[6] P. R. Arantes Gilz, M. Joldes, C. Louembet, and F. Camps, "Stable Model Predictive Strategy for Rendezvous Hovering Phases Allowing for Control Saturation," *Journal of Guidance, Control, and Dynamics*, Vol. 42, No. 8, pp. 1658–1675, 2019.

[7] J. C. Sanchez, C. Louembet, F. Gavilan, and R. Vazquez, "Event-Based Impulsive Control for Spacecraft Rendezvous Hovering Phases," *Journal of Guidance, Control, and Dynamics*, Vol. 44, No. 10, pp. 1794–1810, 2021.

[8] C. Zhao, M. Maestrini, and P. Di Lizia, "Low-Thrust Optimal Control of Spacecraft Hovering for Proximity Operations," *Journal of Guidance, Control, and Dynamics*, Articles in Advance.

[9] C. Roscoe, J. Westphal, and E. Mosleh, "Overview and GNC design of the CubeSat Proximity Operations Demonstration (CPOD) mission," *Acta Astronautica*, Vol. 153, pp. 410–421, 2018.

[10] P. R. Arantes Gilz, "A Matlab®/Simulink® Non-Linear Simulator for Orbital Spacecraft Rendezvous Applications," 2016.

[11] J. Tschauner, "Elliptic Orbit Rendezvous," *AIAA Journal*, Vol. 5, No. 6, pp. 1110–1113, 1967.

[12] K. Yamanaka, and F. Ankersen, "New State Transition Matrix for Relative Motion on an Arbitrary Elliptical Orbit," *Journal of Guidance, Control, and Dynamics*, Vol. 25, No. 1, pp. 60–66, 2002.

[13] A. De Vittori, M. F. Palermo, P. Di Lizia, and R. Armellin, "Low-Thrust Collision Avoidance Maneuver Optimization," *Journal of Guidance, Control, and Dynamics*, Vol. 45, No. 10, pp. 1–15, 2022.

[14] A. Bryson, "Applied Optimal Control: Optimization, Estimation and Control," *CRC Press*, Boca Raton, FL, 2017.